Title

Transition metal-free graphene framework based on disulfide bridges as a Li host material

Authors

Yoo, Young Geun
Park, Soomin
Bae, Seongjun
et al.

Publication Date

2018-09-01

DOI

10.1016/j.ensm.2018.04.007

Peer reviewed

Energy Storage Materials 14 (2018) 238–245

Contents lists available at ScienceDirect

Energy Storage Materials

journal homepage: www.elsevier.com/locate/ensm

Transition metal-free graphene framework based on disulfide bridges as a Li host material

Young Geun Yoo[1], Soomin Park[1], Seongjun Bae, Jongseok Park, Inho Nam, Jongheop Yi*

WCU Program of Chemical Convergence for Energy & Environment, School of Chemical and Biological Engineering, Institute of Chemical Processes, Seoul National University, Seoul 08826, Republic of Korea

ARTICLE INFO

Keywords:
Li ion battery
Graphene
Organic battery
Framework
Disulfides

ABSTRACT

A graphene sulfide framework (GSF) is designed and synthesized *via* a hybridization of graphene and organic compounds for use in electrodes for high-performance Li-ion batteries (LIB). This electrode material is devoid of transition metal and features a layered framework structure that is constructed by the formation of covalent disulfide bonds between organic linker molecules and graphene sheets. This structure capitalizes on the advantageous properties of each of the components in an electrochemical reaction. The structures of GSFs are characterized by Cs-corrected transmission electron microscopy (Cs-TEM), field emission scanning electron microscopy (FE-SEM), and X-ray diffraction (XRD). Depending on current density, the GSF electrodes exhibit two different types of electrochemical behavior during Li incorporation/extraction process, indicating the involvement of multiple Li-incorporation mechanisms. Various types of dithiol organics as linker components are incorporated in the GSF to evaluate the effect of length or structure on the electrochemical properties. The linker-dependent Li storage mechanism is explained based on the results of differential capacity analyses and electrochemical impedance spectroscopy (EIS). The GSF proposed in this study shows promise as an electrode material for a high-performance energy-storage system that is inexpensive and free of transition metals.

1. Introduction

The exploitation of Li chemistry has resulted in great progress in the field of electric energy storage systems, and large-scale electric devices (electric vehicles and grid-energy storage systems) are now operated using Li-ion batteries (LIBs). Despite the advantageous power and energy density of LIBs over other energy storage systems, the surging demand for ever-higher levels of performance drives the continuous development of advanced electrode materials for LIBs. Current LIBs are mainly composed of two types of materials: either graphite or inorganic crystals containing transition metal (TM) species. Among these, the TM-based electrodes feature greater levels of energy density and cyclic stability, which has attracted intensive research on this electrode material [1–17]. However, most TM-based materials have the disadvantageous aspect of gravimetric capacity due to inherently high atomic mass. In addition, detrimental effects on eco-systems and low cost-effectiveness have increased concerns about the use of TM-containing materials [18–20]. Consequently, the development of a TM-free electrode material is highly anticipated for a variety of aspects.

Graphene has been investigated for use as a TM-free electrode material due to its high capacity [21–41]. Although the theoretical capacity of graphene as LIB anodes is usually calculated as high as 744 mAh g^{-1}, which is simply double the value of graphite, many studies have reported that more than 1000 mAh g^{-1} can be achieved via the chemical modification of graphene. The most widely used method for improving the electrochemical activity of graphene involves heteroatom doping with compounds such as nitrogen, boron, and sulfur [21–24]. However, the doping processes usually require high reaction temperatures of approximately 800 °C that demands a high use of energy at great cost. Recently, several studies showed that graphene materials can be functionalized under mild conditions (< 100 °C) using simple synthetic methods (e.g. thiolation, acylation, and Grignard reaction) that are common in the field of organic chemistry [42–44]. Therefore, the introduction of such synthetic methods could be useful for the construction of high-performance graphene-based electrode material at a lower production cost. Recent important researches on the simple organic molecules as LIB electrode material has provided great potential for their synergism with functionalized graphene [45–48].

* Corresponding author. .
E-mail address: jyi@snu.ac.kr (J. Yi).
[1] These authors contributed equally to this work.

https://doi.org/10.1016/j.ensm.2018.04.007
Received 17 January 2018; Received in revised form 27 March 2018; Accepted 6 April 2018
Available online 07 April 2018

In the present study, we developed a graphene sulfide framework (GSF) with graphene sheets connected by disulfide bridges that can act as a TM-free and high-performance anode material for LIBs. We adopted functionalized graphene and organic compounds to serve as building blocks for a GSF. An understanding of the structure-property relationships of the GSF is necessary to achieve the optimized electrochemical performance of a GSF. The gap between graphene layers should be emphasized, as it determines Li ion mobility inside the material and the amount of surface area available for Li adsorption. The introduction of organic compounds for bridging the gap between graphene sheets enables one to control the inter-sheet distance and prevent the undesired restacking of individual sheets. Two essential design criteria include the presence of structural diversity and the existence of functional groups located at both ends of the organic linkers. Those functional groups are supposed to be responsible for the potential-sensitive redox reaction of Li, which affects the voltage profile during Li incorporation/extraction into/from synthesized material. To investigate the effects of the structure of a linker component on electrochemical performance, 1,2-ethanedithiol (EDT), 1,4-benzenedithiol (BDT), biphenyl-4,4'-dithiol (BPDT), and *p*-terphenyl-4,4"-dithiol (TPDT) were used as functional organic linkers in the GSF. The synthesized GSFs showed distinctive electrochemical performance, which depends on linkers that feature reversible cleavage/formation of disulfide bonds upon lithiation/delithiation [49,50]. The optimized GSF exhibited a specific capacity of more than 1000 mAh g^{-1} and stable cyclability during 100 charge-discharge cycles.

2. Materials and methods

2.1. Synthetic method

Graphene oxide (GO) was synthesized using the improved Hummer's method reported by Marcano et al. [51] The pre-treatment of GO with a base solution and the synthesis of thiol-functionalized graphene oxide (SHGO) were in reference to procedures reported by Thomas et al. [52].

2.1.1. Pretreatment of graphene oxide with base solution

500 mg of GO was dispersed in 500 ml of deionized water by sonication for 30 min. Under gentle stirring conditions, 10 ml of a 1.25 M NaOH solution was slowly added until a dark brown color had formed. The solution was stirred at 70 °C for 1 h. The base-treated GO samples were collected by centrifuge at 12,500 rpm for 30 min. After washing with deionized water, the samples were re-dispersed in 500 ml of a 0.05 M HCl solution, and re-stirred at 70 °C for 1 h. After centrifuge and washing by the previously mentioned procedure, the resultant sample was dried under 0.1 Torr vacuum at 60 °C for 12 h. The obtained base-washed GO (bwGO) sample was collected and grinded.

2.1.2. Synthesis of thiol-functionalized graphene oxide (SHGO)

200 mg of bwGO in 50 ml DMSO solution was sonicated for 1 h. The dispersed solution was sealed and then moved into an Ar-filled glove box. After adding 20 mg of potassium thioacetate (CH_3COSK), the solution was tightly sealed and reacted at 50 °C for 5.5 h. After cooling to room temperature (RT), 10 ml of a 1 M HCl solution was added and then centrifuged at 12,500 rpm for 30 min. The sample was washed according to the following procedure: acetone (20 min, 3 times), diethyl ether (10 min, 2 times) and deionized water (2 h, 3 times). The SHGO was finally obtained after drying the sample under 0.1 Torr vacuum at RT.

2.1.3. Disulfide-linking between SHGO and linker molecules

The disulfide bond formation method reported by M. Kirihara et al. was adopted [53]. First, 100 mg of SHGO was dispersed in 30 ml ethyl acetate ($CH_3CO_2C_2H_5$, EtOAc). After dispersion by intensive sonification (duty cycle: 50 %, output: 60 W) for 10 min, the solution was cooled at RT. The amounts of added linker molecules were calculated

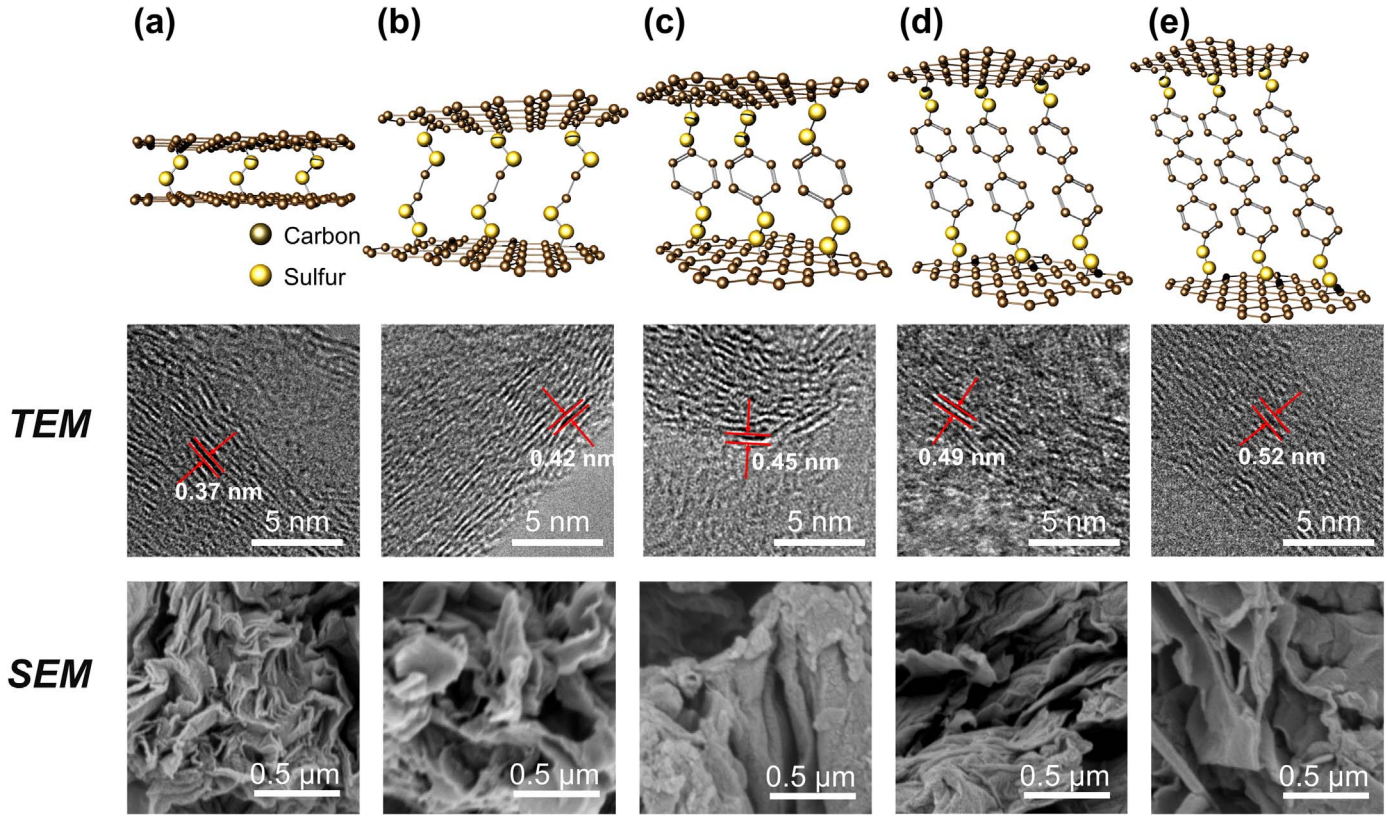

Fig. 1. Graphical images, TEM and SEM images of (a) SSGO, (b) GSF/EDT, (c) GSF/BDT, (d) GSF/BPDT and (e) GSF/TPDT.

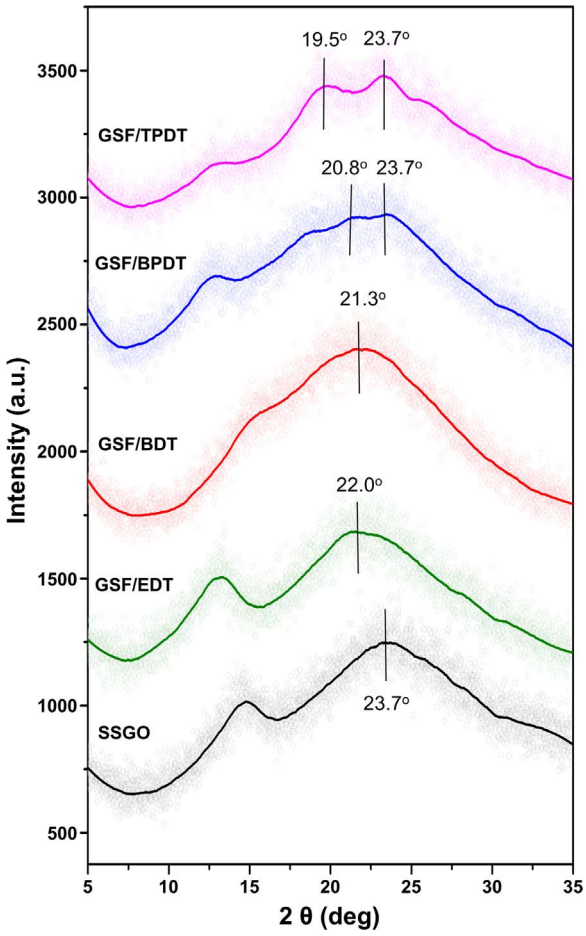

Fig. 2. XRD patterns of SSGO, GSF/EDT, GSF/BDT, GSF/BPDT and GSF/TPDT from 5° to 35°. Raw data are expressed as hollow dots and solid lines indicate smoothed values. Adjacent-averaging was utilized for smoothing, and the point of windows was set as 50.

as follows: 20.5, 31.5, 42.4, and 13.6 mg of BDT, BPDT, TPDT and EDT, respectively. After a linker was added, the SHGO/linker mixed solution was stirred for 10 min. After adding 3 mg NaI with stirring for 10 min, 0.22 ml of 30% H_2O_2 was added, and was stirred for 24 h at room temperature. The synthesized sample was membrane-filtered and washed with 10 ml EtOAc, 20 ml ethanol, and 10 ml acetone. After drying under 0.1 Torr vacuum at 60 °C for 12 h, the resultant GSF samples were obtained. A schematic diagram of the synthetic procedures for SHGO and GSF is shown in Fig. S1.

2.2. Electrochemical measursements

All of the electrodes for the electrochemical performance measurement were fabricated by mixing active material:Super P:poly(vinylidene difluoride) (PVdF, Sigma-Aldrich) in an 8:1:1 weight ratio. The mixed components were dispersed homogeneously in a few drops of *N*-methyl-2-pyrrolidone (NMP) in an agate mortar. The dark-greyish slurry mixtures were uniformly caste onto Cu foils *via* doctor-blading and dried under 0.1 Torr vacuum at 60 °C for 12 h. Then the electrodes were roll-pressed, cut into 1 cm^2 round discs, and assembled into a button-type coin cell (CR2032). Li foil (0.75 mm thickness, Alfa Aesar) and 1.15 M $LiPF_6$ in a 2:4:4 volumetric ratio of ethyl carbonate/ethyl-methyl carbonate/dimethyl carbonate solution were used as counter electrode and electrolyte, respectively. Galvanostatic charge/discharge properties were characterized with multichannel battery cycling equipment (WBCS3000, WonATech). Electrochemical impedance spectroscopy (EIS) was conducted using potentiostat equipment (ZIVE SP2, WonATech). The electrochemical parameters of the equivalent circuit were obtained using ZMAN software.

2.3. Characterizations

The gap distances of the GSFs were analyzed *via* Cs-corrected Transmission electron microscopy (Cs-TEM, JEM-ARM200F). Also, field-emission scanning electron microscopy (FESEM, AUGIRA) was used to analyze the surface morphology. To analyze the elemental components and chemical states of the samples, X-ray photoelectron spectroscopy (XPS, Sigma Probe, Thermo) was performed. An X-ray

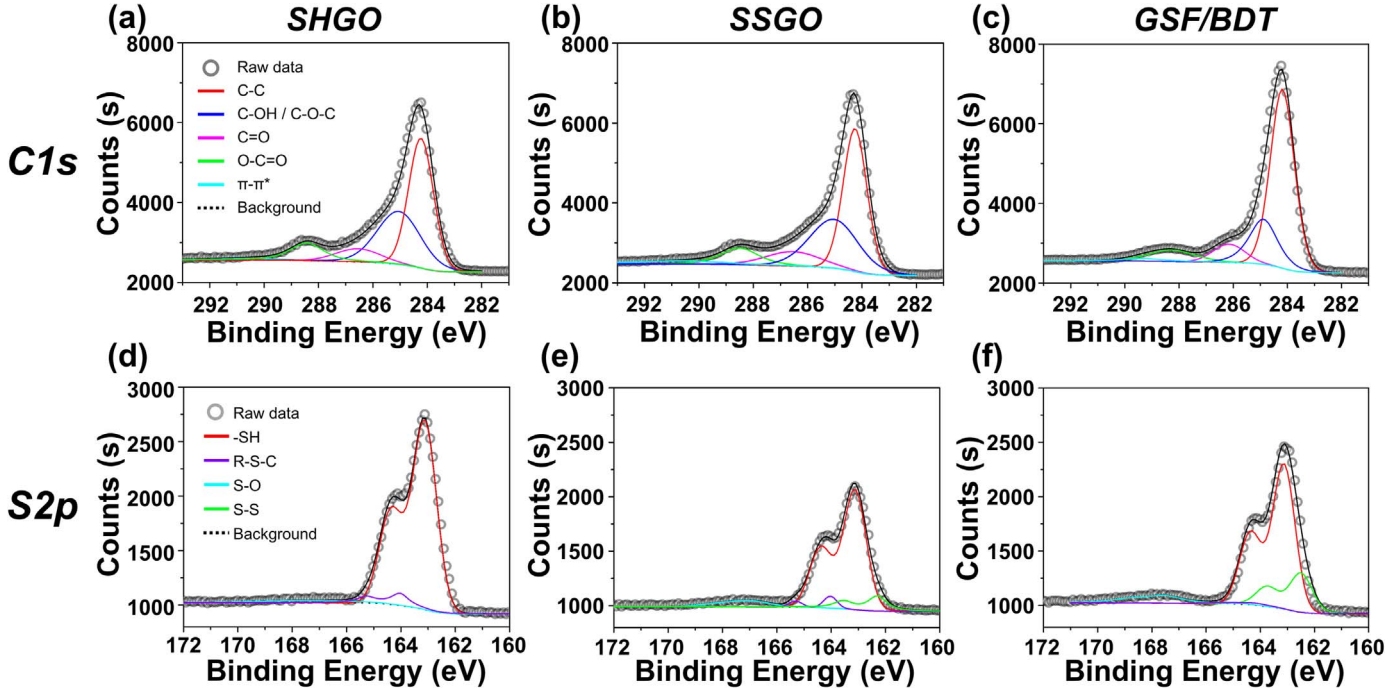

Fig. 3. XPS spectra and deconvoluted peaks for C1s and S2p of (a) SHGO, (b) SSGO and (c) GSF/BDT.

diffractometer (XRD, Rigaku, D/max-2200, Cu Kα1 radiation) was used to investigate the diffraction patterns of the synthesized samples. BET surface areas were measured using a Micrometrics ASAP 2010 instrument.

3. Results & discussion

Fig. 1 shows a graphical image of the GSFs with different linkers along with their TEM and SEM images. As a control sample, a GSF without a linker was also prepared for comparison, and is referred to as SSGO. As shown in the TEM images, the gaps between the graphene layers became wider as longer linker molecules were incorporated in the GSFs (SSGO = 0.37 nm, GSF/EDT = 0.42 nm, GSF/BDT = 0.45 nm, GSF/BPDT = 0.49 nm, GSF/TPDT = 0.52 nm). The observed gap distance values of the GSFs showed differences in the molecular length of the adopted linkers. The bonding angle of -S-S- was 103°, so the linkers were attached between graphene layers in an inclined configuration, rather than in a straight-standing form. In SEM analysis, all of the samples showed highly porous morphologies, which means that restacking between graphene sheets was prevented during the synthesis processes for all samples.

Fig. 2 shows the XRD patterns of the GSFs. The main peak positions of SSGO, GSF/EDT, GSF/BDT, GSF/BPDT, and GSF/TPDT appeared at 23.7, 22.0, 21.3, 20.8, and 19.5°, respectively. These results correlated well with TEM analysis showing that the gap distances widened as longer linkers were used. The diffraction patterns at 23.7° corresponded to GSF/BPDT and GSF/TPDT because of the partial nature of the disulfide bond formation between SHGOs when there was no insertion of either linkers or unreacted thiols. As described above, the main diffraction peak of SSGO was observed at 23.7°. However, this unspecific formation of a disulfide bond was observed neither in GSF/EDT nor in GSF/BDT. Diffraction patterns of other intermediate materials such as graphite, GO, bwGO, and SHGO are also shown in Fig. S2.

XPS analysis was used to observe the chemical state of carbon and sulfur before and after the disulfide formation reaction. Fig. 3(a), (b), and (c) show the C1s spectra of SHGO, SSGO and GSF/BDT, respectively. Each of the deconvoluted peaks in these spectra represent commonly known functional groups on GO such as C-C bonds (284.2 eV), hydroxyls (285.4 eV), carbonyls (286.8 eV), and esters (288.7 eV). The C1s spectra of SHGO and SSGO show no remarkable difference in either peak position or intensity, which means that disulfide bond formation had a negligible effect on the chemical state of the carbon-containing functional groups on SHGO. In GSF/BDT, however, a higher peak intensity of C-C was observed compared with that of the other two materials, which was due to the incorporation of aromatic ring-containing linker molecules. Fig. 3(d), (e) and (f) are the results of the S2p analyses of SHGO, SSGO and GSF/BDT, respectively. To distinguish the peaks corresponding to -SH (163.1 and 164.3 eV) and -S-S- (162.1 and 163.0 eV), normalized S2p peaks of these 3 materials from 161 to 166 eV are compared in Fig. S3. A slight shift in the peak positions of SSGO and GSF/BDT to a lower binding energy verified that even -SH was dominant from among all three materials, and that a disulfide bond was partially formed in SSGO and even more so in GSF/BDT. Therefore, the peak deconvolution was proceeded based on this observation. The results of S2p analysis were also utilized to quantify the sulfur content in SHGO. The atomic ratio of sulfur in SHGO was calculated as 4.2%. Based on this value, we determined the amount of linkers required for the construction of GSFs in order to acquire a molar ratio of 1:1 for the thiol groups in SHGO and linkers.

To evaluate the Li storage performances of the synthesized samples, half-cell Galvanostatic charge/discharge tests were carried out using Li metal as an anode. Fig. 4(a) shows the first cycle charge/discharge profiles of samples at a current density of 0.05 A g^{-1}, and a potential window from 0.01 V to 3.0 V. Discharge capacities of 703, 1055, 778, 725, and 892 mAh g^{-1} during the first cycle were recorded for SSGO, GSF/BDT, GSF/BPDT, GSF/TPDT, and GSF/EDT, respectively. All samples showed analogous profiles and a sloped potential plateau below 1.0 V during charge and discharge. The electrochemical behavior of disulfide bonds with Li ions have been well established in previous reports, and the overpotential between oxidation and reduction is relatively high (~1.6 V) due to the low reaction kinetics [54]. Considering this effect, the discharge plateau that appeared at 1.0 V was due to the lithium-sulfur bond formation. The redox behavior of disulfide was observed in differential analysis (Fig. 5(a) and (b)). In the first cycle, all samples showed a low level of Coulombic efficiency (52.8 ~ 68.8 %). The *ex-situ* XPS revealed that the formation of Li_2CO_3, with a main component composed of a solid electrolyte interphase (SEI), on the GSFs during charge/discharge cycles (Fig. S4). Therefore, a high irreversible capacity among all materials during the first cycle was due to the formation of SEI. After the first cycle, the highly reversible nature of lithiation and delithiation was maintained. The charge/discharge profiles of samples at various current densities are presented

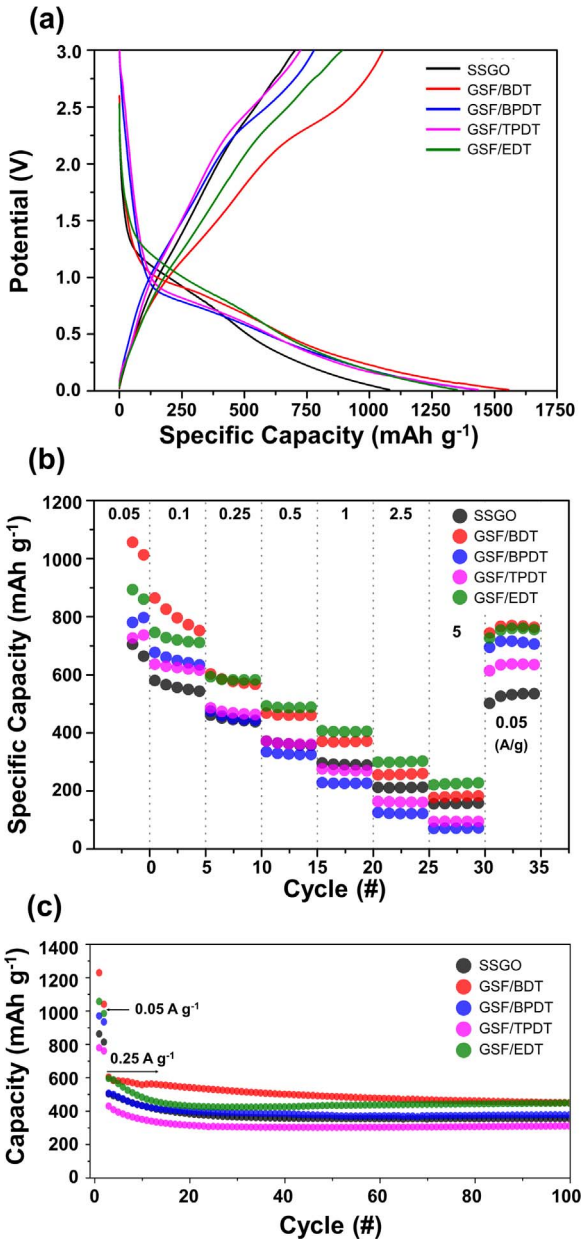

Fig. 4. Galvanostatic charge/discharge results of SSGO and GSFs: (a) 1st cycle charge/discharge profiles, (b) Specific capacities measured at various current densities from 0.05 to 5 A g^{-1} for 5 cycles each and (c) long term stability test.

in Fig. S5, and the initial charge/discharge profiles and rate capability of graphite, bwGO, and SHGO are shown in Fig. S6.

Charge/discharge testing was performed at various current densities to evaluate the rate capability of the GSFs (Fig. 4(b)). The GSFs with long linkers, GSF/BPDT and GSF/TPDT, showed a relatively lower capacity in all ranges of current rates due to the higher amount of electrochemically inactive weight of the aromatic rings in the linker molecules. At relatively low current densities, 0.05 and 0.1 A g^{-1}, GSF/BDT showed the highest specific capacity, followed by GSF/EDT, GSF/BPDT, GSF/TPDT, and SSGO. As current density increased by more than 0.25 A g^{-1}, however, the specific capacity of GSF/EDT began to overtake that of GSF/BDT. Also, GSF/BPDT and GSF/TPDT showed values that were even lower than those of SSGO. Details of these results will be discussed later.

Fig. 4(c) indicates the long cyclic stability of the SSGO and GSFs. The cells were first cycled at 0.05 A g^{-1} for 2 cycles to promote stabilization, and were then cycled repeatedly at 0.25 A g^{-1}. After 100 cycles, GSF/BDT, GSF/BPDT, and GSF/TPDT retained 78.1, 74.0, and 75.8% of their initial capacities, respectively. However, the reversible capacity of GSF/EDT was quickly degraded in the first 10 cycles, which could be attributed to the innate structural instability of EDT compared with other linkers containing aromatic rings.

As described above, the rate performances differed among the GSFs depending on current density, particularly between GSF/BDT and GSF/EDT. To clarify the Li storage mechanisms that depended on current rates, N_2 adsorption and desorption analyses were first carried out to measure the BET surface area (Table S1). There were no remarkable differences in the surface areas between the GSFs, and it could be assumed that the discrepancies in the Li storage performances of GSFs were not significantly affected by the differences in surface areas. Note that no morphological differences were found among the materials, as discussed in SEM analysis (Fig. 1). Fig. 5(a) and (b) represent differential capacities during delithiation at 0.05 A g^{-1} and 0.25 A g^{-1}, respectively. At 0.05 A g^{-1}, cathodic peaks corresponding to disulfide bond formations (-SLi + LiS- → -S-S- + $2Li^+$) were observed, while the peaks were significantly attenuated at 0.25 A g^{-1}. We speculated that a threshold of current density exists between 0.05 and 0.25 A g^{-1}, which could be related to the accessibility of Li ions toward the interior of GSF structures when thiol redox moieties are present.

To obtain more evidence on linker-dependent Li storage mechanisms, we performed XPS analyses with 4 types of GSF/BDT which include the electrodes charged and discharged at low (0.05 A g^{-1}) and high (0.25 A g^{-1}) current densities. Fig. S7 shows the S2p spectra of the prepared electrodes. Even at a low signal-to-noise ratio, we were able to find the signal corresponding to an S-Li bond (near 160 eV) from the electrode that was discharged at 0.05 A g^{-1} (Note that the low signal-to-noise ratio of XPS data is due to the low atomic concentration of sulfur in GSF). However, there were no noticeable signals in other samples. The XPS data indicates that the formation of S-Li bonds by Li oxidation occurred only within the electrode discharged at low current density. Considering that disulfide bridges exist between the graphene layers in GSFs, this result supports the idea that Li diffusions through interstitial graphene layers and subsequent redox reactions are prominent at low current density. This phenomena is also well-correlated with the previous reports on graphene anode materials for LIBs, whereby the Li storage mechanism of graphene varies depending on the current density [33,34].

Electrochemical impedance spectroscopy (EIS) analyses were carried out to analyze the detailed resistive factors in the GSF structures. Fig. 5(c) and (d) represent the acquired Nyquist plots of SSGO and GSFs, respectively, for application of the equivalent electrochemical circuit model. The simulated parameters are shown in Table 1, where R_e is the equivalent series resistance, R_{ic} is the charge transfer

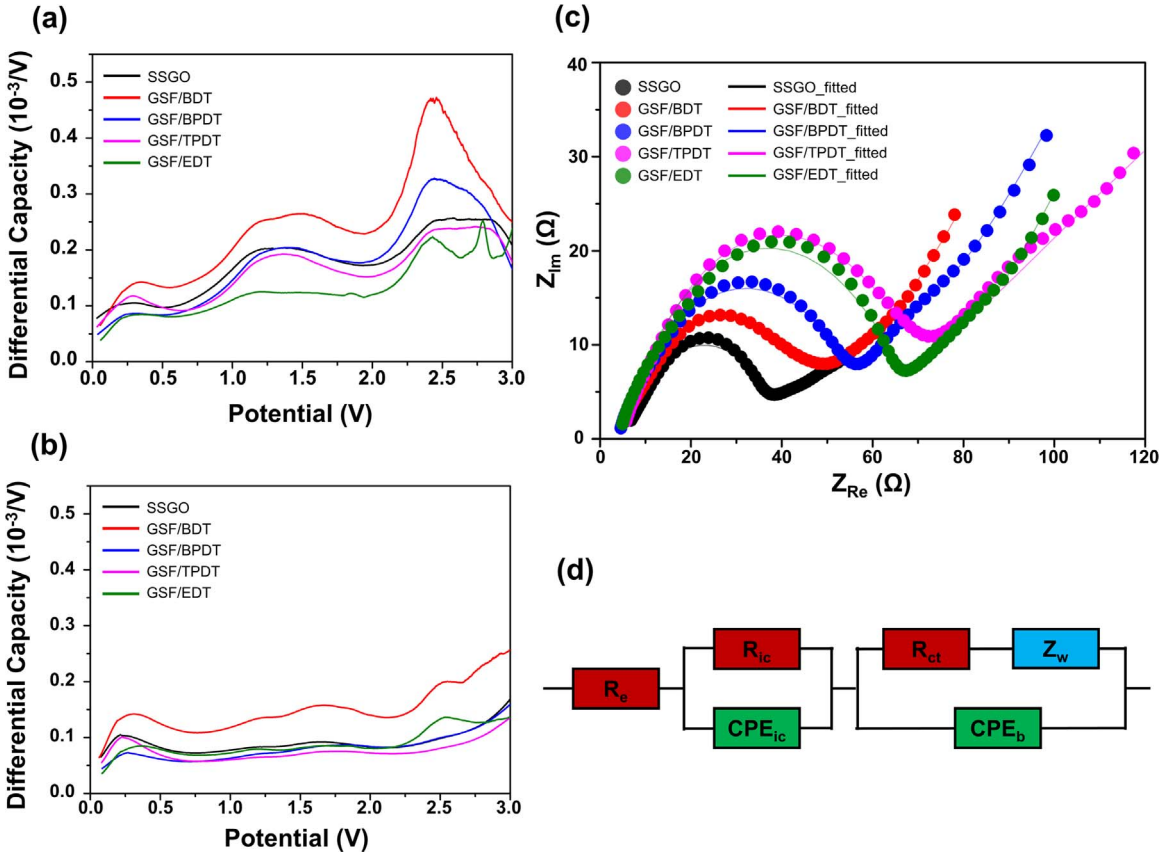

Fig. 5. (a,b) Differential capacity analyses during Li extraction at current density of (a) 50 mA g^{-1} and (b) 250 mA g^{-1}, (c) Nyquist plots analyzed at frequencies ranging from 100 mHz to 100 kHz at a 10 mV amplitude and (d) applied equivalent circuit model for parameter fitting.

Table 1
Resultant parameters of EIS data by fitting simulations.

	R_e	R_{ic}	R_{ct}	A_w
SSGO	5.89	35.00	6.37	5.96×10^2
GSF/EDT	4.15	67.69	5.69	3.52×10^2
GSF/BDT	2.96	24.46	42.35	2.90×10^2
GSF/BPDT	3.71	55.82	16.44	2.96×10^2
GSF/TPDT	2.79	54.06	35.65	2.79×10^2

resistance between intercrystallites. Because the electrochemically active part in GSF is graphene layers, R_{ic} is assigned as charge transfer resistance between graphene sheets across the linker molecules. R_{ct} is the charge transfer resistance between an electrode and its active material, and A_w is the Warburg coefficient which represents the mass transfer resistance, which is defined as follows:

$$Aw = \frac{RT}{An^2F^2\theta C\sqrt{2D}}$$

where R is the gas constant, T is the temperature, A is the diffusion area, n is the valency, F is the Faraday constant, C is Li ion concentration, D is the diffusion coefficient of Li ion, and θ denotes the fraction of the reduced and oxidized species present.

The high R_{ic} that is obvious in GSF/EDT could be attributable to a linker molecule without a conjugated aromatic structure. However, considerable values for R_{ic} were also observed in GSF/BPDT and GSF/TPDT. As explained above, during the synthesis of the GSF, the slow reaction kinetics of BPDT and TPDT with SHGOs created a small population of linker pillars between the graphene layers in GSF/BPDT and GSF/TPDT. Consequently, the reduced amount of organic linker resulted in loosely packed structures for GSF/BPDT and GSF/TPDT. The R_{ct} in GSF/BDT had the highest value among the samples. It is possible that the lower graphene content in GSF/BDT, compared with that in SSGO and other GSFs, induces distinctive surface properties (e.g. hydrophobicity, wettability). As the molecular length of the linkers increased, the A_w values tended to decrease, however, there was a negligible difference between GSF/BDT, GSF/BPDT and GSF/TPDT. To summarize the EIS results, GSF/BDT was favorable in terms of inter-sheets charge transfer and mass transfer, whereas GSF/EDT had the most favorable level of charge transfer between active material and electrode.

Based on the differential analysis, EIS and XPS observations, multiple Li ion storage mechanisms were proposed for the GSFs (Fig. 6). Li adsorption on the inner and outer surfaces of graphene and redox reactions with disulfides are possible mechanisms. Both Li adsorption on the inner surface and redox reactions with disulfides should be based on the precondition that the Li ions can diffuse into the graphene layers. Thus, these mechanisms can be categorized into two forms: Li insertion between layers and adsorption on the surface. At low current densities, Li insertion between layers and either the subsequent redox reaction or adsorption occupies a large portion of the overall Li storage. The lower specific capacities of GSF/BPDT and GSF/TPDT are due to the higher content of the electrochemically inactive mass within linker molecules, as discussed above (Fig. 3(b)). By contrast, although BDT has a higher molecular weight than EDT, the specific capacity of GSF/BDT surpasses that of GSF/EDT. As presented in the EIS analyses, GSF/EDT shows R_{ic} and A_w values that are higher than those of GSF/BDT, which indicates that the shorter molecular length and structural instability of EDT increases the electron/mass-transfer resistance within GSF/EDT. Therefore, at low current density, GSF/BDT represents the optimized structure of the GSF by means of the structural stability of the aromatic linker molecules and moderate amounts of electrochemically inactive elements. The lowest specific capacity of SSGO can also be explained by the fact that, without linker molecules, it is possible to store only small amounts of Li between the graphene layers of SSGO. On the other hand, adsorption of Li ions on the outer surface of materials becomes dominant at relatively high current density. Under this condition, the amount of Li insertion between the layers decreases, and, consequently, the weights of electrochemically inactive elements determine the specific capacities of materials. Therefore, GSF/EDT showed a higher value of specific capacity compared with that of GSF/BDT. The SSGO was relatively less affected by increases in the current density, which enabled it to exhibit superior specific capacities over GSFs within a high current domain (> 0.25 A g^{-1}).

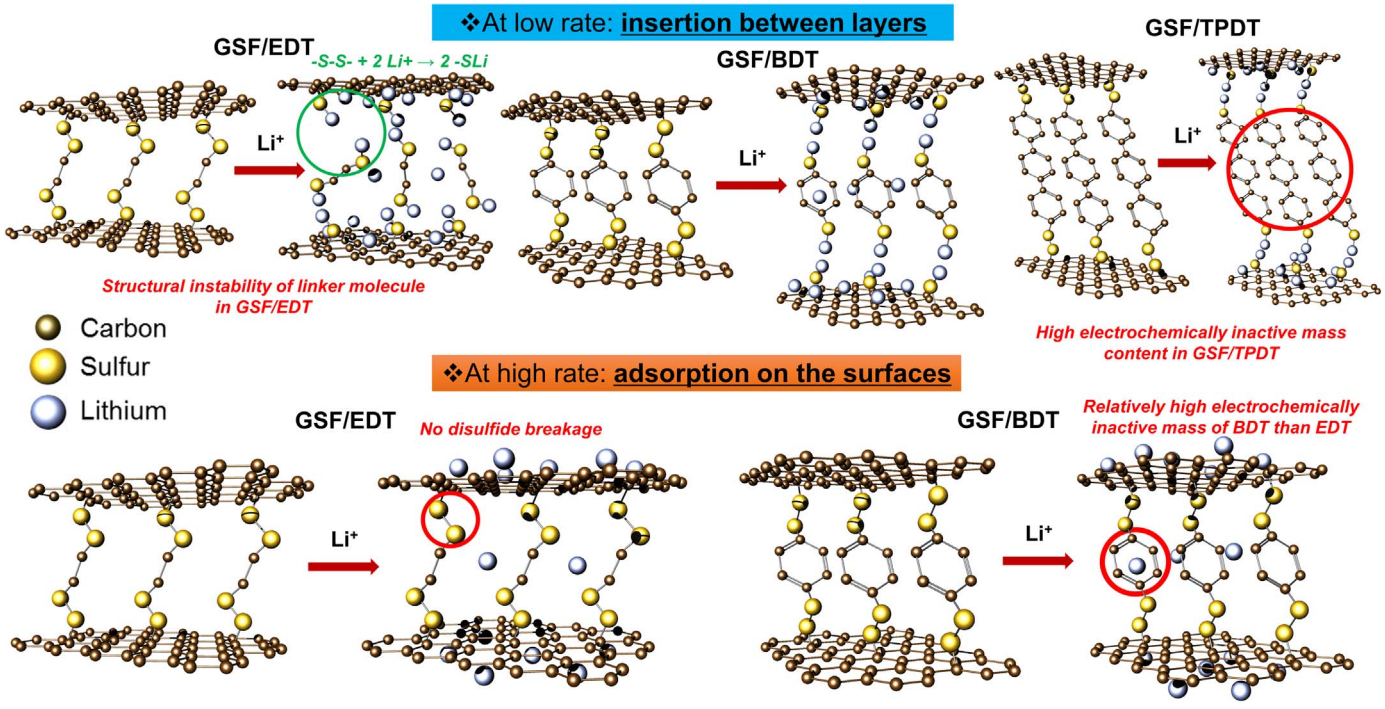

Fig. 6. Schematic illustrations explaining the Li^+ storing mechanisms with various GSF materials at different current rates.

4. Conclusions

In the present research, a GSF electrode was proposed as an advanced type of graphene-based electrode material with enhanced Li electroactivity. The synthesized GSF showed a specific capacity of more than 1000 mAh g^{-1} at 0.05 A g^{-1} of current density. Considering its economic feasibility, eco-friendly, and excellent performances, GSF electrodes provide competitive Li storage performance compared with those of graphene-based anode materials reported previously (Table S2). When evaluating the effect of various linker molecules on electrochemical performance, GSF/BDT and GSF/EDT had the highest specific capacities at low and high current densities, respectively. When analyzing collected data from differential capacity analysis and EIS, structural stability and a minimized electrochemically inactive mass of linker molecules are the two most important factors that will increase the Li storage performance of a GSF. This research marks the first attempt to design GSF material for use in Li host materials. We believe that further optimization of the GSF could strengthen its candidacy as an advanced TM-free electrode material. For example, the large amount of thiol functionalization on the graphene surface enables a higher population of linker molecules, and will be valued greatly for the further enhancement of Li storage performance. In addition, the use of nano-sized functional graphene and the additional functionality of organic linkers would also be beneficial to the GSF. Now that graphene is used as electrode material for other energy storage systems such as Na-ion batteries and supercapacitors, the GSF and its structural tunability could be useful in achieving desired performances in such systems.

Acknowledgements

This work was supported by the National Research Foundation of Korea (NRF) grant funded by the Korea government (MEST) (NRF-2016R1E1A1A01942936).

Appendix A. Supporting information

Supplementary data associated with this article can be found in the online version at doi:10.1016/j.ensm.2018.04.007.

References

[1] W.-Y. Li, L.-N. Xu, J. Chen, Co_3O_4 nanomaterials in lithium-ion batteries and gas sensors, Adv. Funct. Mater. 15 (2005) 851–857.
[2] J. Chen, L. Xu, W. Li, X. Gou, α-Fe_2O_3 nanotubes in gas sensor and lithium-ion battery applications, Adv. Mater. 17 (2005) 582–586.
[3] H. Liu, G. Wang, J. Liu, S. Qiao, H. Ahn, Highly ordered mesoporous NiO anode material for lithium ion batteries with an excellent electrochemical performance, J. Mater. Chem. 21 (2011) 3046.
[4] X.W. Lou, Y. Wang, C. Yuan, J.Y. Lee, L.A. Archer, Template-free synthesis of SnO_2 hollow nanostructures with high lithium storage capacity, Adv. Mater. 18 (2006) 2325–2329.
[5] A.R. Armstrong, G. Armstrong, J. Canales, R. García, P.G. Bruce, Lithium-ion intercalation into TiO_2-B nanowires, Adv. Mater. 17 (2005) 862–865.
[6] P. Poizot, S. Laruelle, S. Grugeon, L. Dupont, J.-M. Tarascon, Nano-sized transition-metal oxides as negative-electrode materials for lithium-ion batteries, Nature 407 (2000) 496–499.
[7] H.B. Wu, J.S. Chen, H.H. Hng, X.W. Lou, nanostructured metal oxide-based materials as advanced anodes for lithium-ion batteries, Nanoscale 4 (2012) 2526.
[8] E. Ferg, R.J. Gummow, A. de Kock, M.M. Thackeray, Spinel anodes for lithium-ion batteries, J. Electrochem. Soc. 141 (1994) L147–L150.
[9] K. Mizushima, P.C. Jones, P.J. Wiseman, J.B. Goodenough, Li_xCoO_2 (0 < x ≤ l): a new cathode material for batteries of high energy density, Mat. Res. Bull. 15 (1980) 783–789.
[10] S.-Y. Chung, J.T. Bloking, Y.-M. Chiang, Electronically conductive phospho-olivines as lithium storage electrodes, Nat. Mater. 1 (2002) 123–128.
[11] H.-W. Lee, P. Muralidharan, R. Ruffo, C.M. Mari, Y. Cui, D.K. Kim, Ultrathin spinel $LiMn_2O_4$ nanowires as high power cathode materials for Li-ion batteries, Nano Lett. 10 (2010) 3852–3856.
[12] T. Ohzuku, A. Ueda, M. Nagayama, Electrochemistry and structural chemistry of $LiNiO_2$ (R3m) for 4 volt secondary lithium cells, J. Electrochem. Soc. 140 (1993) 1862–1870.
[13] Y. Zhu, X. Han, Y. Xu, Y. Liu, S. Zheng, K. Xu, L. Hu, C. Wang, Electrospun, Sb/C fibers for a stable and fast sodium-ion battery anode, ACS Nano 7 (2013) 6378–6386.
[14] M.N. Obrovac, V.L. Chevrier, Alloy negative electrodes for Li-ion batteries, Chem. Rev. 114 (2014) 11444–11502.
[15] C.K. Chan, H. Peng, G. Liu, K. McIlwrath, X.F. Zhang, R.A. Huggins, Y. Cui, High-performance lithium battery anodes using silicon nanowires, Nat. Nanotechnol. 3 (2008) 31–35.
[16] X.B. Zhao, G.S. Cao, C.P. Lv, L.J. Zhang, S.H. Hu, T.J. Zhu, B.C. Zhou, Electrochemical properties of some Sb or Te based alloys for candidate anode of lithium-ion batteries, J. Alloy. Compd. 315 (2001) 265–269.
[17] W.-J. Zhang, A review of the electrochemical performance of alloy anodes for lithium-ion batteries, J. Power Sources 196 (2011) 13–24.
[18] M. Valko, H. Morris, M.T.D. Cronin, Metals, toxicity and oxidative stress, Curr. Med. Chem. 12 (2005) 1161–1208.
[19] P.C. Nagajyoti, K.D. Lee, T.V.M. Sreekanth, Heavy metals, occurrence and toxicity for plants: a review, Environ. Chem. Lett. 8 (2010) 199–216.
[20] G.J. Brewer, Risks of copper and iron toxicity during aging in humans, Chem. Res. Toxicol. 23 (2010) 319–326.
[21] Z.-S. Wu, W. Ren, L. Xu, F. Li, H.-M. Cheng, Doped graphene sheets as anode materials with superhigh rate and large capacity for lithium ion batteries, ACS Nano 5 (2011) 5463–5471.
[22] Y. Zhao, C. Hu, Y. Hu, H. Cheng, G. Shi, L. Qu, A versatile, ultralight, nitrogen-doped graphene framework, Angew. Chem. Int. Ed. 51 (2012) 11371–11375.
[23] W. Ai, Z. Luo, J. Jiang, J. Zhu, Z. Du, Z. Fan, L. Xie, H. Zhang, W. Huang, T. Yu, Nitrogen and sulfur codoped graphene: multifunctional electrode materials for high-performance Li-ion batteries and oxygen reduction reaction, Adv. Mater. 26 (2014) 6186–6192.
[24] J. Yang, X. Zhou, D. Wu, X. Zhao, Z. Zhou, S-doped n-rich carbon nanosheets with expanded interlayer distance as anode materials for sodium-ion batteries, Adv. Mater. 29 (2017) 1604108.
[25] J. Xu, I.-Y. Jeon, H.-J. Choi, S.-J. Kim, S.-H. Shin, N. Park, L. Dai, J.-B. Baek, Metalated graphene nanoplatelets and their uses as anode materials for lithium-ion batteries, 2D Mater. 4 (2017) 014002.
[26] Y. Xu, Z. Lin, Z. Zhong, X. Huang, N.O. Weiss, Y. Huang, X. Duan, Holey graphene frameworks for highly efficient capacitive energy storage, Nat. Commun. 5 (2014) 4554–4561.
[27] H. An, Y. Li, Y. Gao, C. Cao, J. Han, Y. Feng, W. Feng, Free-standing fluorine and nitrogen co-doped graphene paper as a high-performance electrode for flexible sodium-ion batteries, Carbon 116 (2017) 338–346.
[28] J.H. Choe, N.R. Kim, M.E. Lee, H.J. Yoon, M.Y. Song, H.-J. Jin, Y.S. Yun, Flexible graphene stacks for sodium-ion storage, ChemElectroChem 4 (2017) 716–720.
[29] C.M. Subramaniyam, K.A. Deshmukh, Z. Tai, N. Mahmood, A.D. Deshmukh, J.B. Goodenough, S.X. Dou, H.K. Liu, 2D layered graphitic carbon nitride sandwiched with reduced graphene oxide as nanoarchitectured anode for highly stable lithium-ion battery, Electrochim. Acta 237 (2017) 69–77.
[30] Y. Sang, Y. Zhou, H. Xie, C. Wang, L. Song, Assembling and nanocutting graphene/CNT sponge for improved lithium-ion batteries, Ionics 23 (2017) 1329–1336.
[31] C. Liu, X. Liu, J. Tan, Q. Wang, H. Wen, C. Zhang, Nitrogen-doped graphene by all-solid-state ball-milling graphite with urea as a high-power lithium ion battery anode, J. Power Sources 342 (2017) 157–164.
[32] R.P. Panmand, P. Patil, Y. Sethi, S.R. Kadam, M.V. Kulkarni, S.W. Gosavi, N.R. Munirathnam, B.B. Kale, Unique perforated graphene derived from Bougainvillea flowers for high-power supercapacitors: a green approach, Nanoscale 9 (2017) 4801–4809.
[33] Z. Fan, J. Yan, G. Ning, T. Wei, L. Zhi, F. Wei, Porous graphene networks as high performance anode materials for lithium ion batteries, Carbon 60 (2013) 538–561.
[34] E. Yoo, J. Kim, E. Hosono, H.-S. Zhou, T. Kudo, I. Honma, Large reversible li storage of graphene nanosheet families for use in rechargeable lithium ion batteries, Nano Lett. 8 (2008) 2277–2282.
[35] D. Pan, S. Wang, B. Zhao, M. Wu, H. Zhang, Y. Wang, Z. Jiao, Li storage properties of disordered graphene nanosheets, Chem. Mater. 21 (2009) 3136–3142.
[36] Z.-J. Fan, J. Yan, T. Wei, G.-Q. Ning, L.-J. Zhi, J.-C. Liu, D.-X. Cao, G.-L. Wang, F. Wei, Nanographene-constructed carbon nanofibers grown on graphene sheets by chemical vapor deposition: high-performance anode materials for lithium ion batteries, ACS Nano 5 (2011) 2787–2794.
[37] R. Mukherjee, A.V. Thomas, A. Krishnamurthy, N. Koratkar, Photothermally reduced graphene as high-power anodes for lithium-ion batteries, ACS Nano 6 (2012) 7867–7878.
[38] W. Lv, Z. Li, Y. Deng, Q.-H. Yang, F. Kang, Graphene-based materials for electrochemical energy storage devices: opportunities and challenges, Energy Storage Mater. 2 (2016) 107–138.
[39] P. Lian, X. Zhu, S. Liang, Z. Li, W. Yang, H. Wang, Large reversible capacity of high quality graphene sheets as an anode material for lithium-ion batteries, Electrochim. Acta 55 (2010) 3909–3914.
[40] P. Guo, H. Song, X. Chen, Electrochemical performance of graphene nanosheets as anode material for lithium-ion batteries, Electrochem. Commun. 11 (2009) 1320–1324.
[41] X. Li, D. Geng, Y. Zhang, X. Meng, R. Li, X. Sun, Superior cycle stability of nitrogen-doped graphene nanosheets as anodes for lithium ion batteries, Electrochem. Commun. 13 (2011) 822–825.
[42] K. Bhowmik, A. Chakravarty, U. Manju, G. De, A. Mukherjee, Carboxylic acid terminated, solution exfoliated graphite by organic acylation and its application in drug delivery, J. Chem. Sci. 128 (2016) 1345–1354.
[43] D.D. Chronopoulos, A. Bakandritsos, P. Lazar, M. Pykal, K. Čépe, R. Zbořil, M. Otyepka, High-yield alkylation and arylation of graphene via Grignard reaction with fluorographene, Chem. Mater. 29 (2017) 926–930.

[44] K. Muthoosamy, S. Manickam, State of the art and recent advances in the ultrasound-assisted synthesis, exfoliation and functionalization of graphene derivatives, Ultrason. Sonochem. 39 (2017) 478–493.
[45] S. Wang, L. Wang, K. Zhang, Z. Zhu, Z. Tao, J. Chen, Organic $Li_4C_8H_2O_6$ nanosheets for lithium-ion batteries, Nano Lett. 13 (2013) 4404–4409.
[46] B. Häupler, T. Hagemann, C. Friebe, A. Wild, U.S. Schubert, Dithiophenedione-containing polymers for battery applications, ACS Appl. Mater. Interfaces 7 (2015) 3473–3479.
[47] B. Häupler, A. Wild, U.S. Schubert, Carbonyls: powerful organic materials for secondary batteries, Adv. Energy Mater. 5 (2015) 1402034.
[48] Y. Liang, Z. Tao, J. Chen, Organic electrode materials for rechargeable lithium batteries, Adv. Energy Mater. 2 (2012) 742–769.
[49] M. Pepels, I. Filot, B. Klumperman, H. Goossens, Self-healing systems based on disulfide-thiol exchange reactions, Polym. Chem. 4 (2013) 4955–4965.
[50] J. Canadell, H. Goossens, B. Klumperman, Self-healing materials based on disulfide links, Macromolecules 44 (2011) 2536–2541.
[51] D.C. Marcano, D.V. Kosynkin, J.M. Berlin, A. Sinitskii, Z. Sun, A. Slesarev, L.B. Alemany, W. Lu, J.M. Tour, Improved synthesis of graphene oxide, ACS Nano 4 (2010) 4806–4814.
[52] H.R. Thomas, A.J. Marsden, M. Walker, N.R. Wilson, J.P. Rourke, Sulfur-functionalized graphene oxide by epoxide ring-opening, Angew. Chem. Int. Ed. 53 (2014) 7613–7618.
[53] M. Kirihara, Y. Asai, S. Ogawa, T. Noguchi, A. Hatano, Y. Hirai, A mild and environmentally benign oxidation of thiols to disulfides, Synthesis 21 (2007) 3286–3289.
[54] M. Liu, S.J. Visco, L.C. de Jonghe, Electrochemical properties of organic disulfide/thiolate redox couples, J. Electrochem. Soc. 136 (1989) 2570–2575.